Theoretical and Applied Fracture Mechanics 143 (2026) 105473

Contents lists available at ScienceDirect

Theoretical and Applied Fracture Mechanics

journal homepage: www.elsevier.com/locate/tafmec

Designing for toughness: How substrate stiffness controls crack path and effective engagement of toughening layers in adhesively bonded CFRP joints

R. A.A. Lima [a,b,*], S. Teixeira de Freitas [a,b]

[a] IDMEC, Instituto Superior Técnico, Lisbon, Portugal
[b] Faculty of Aerospace Engineering, Delft University of Technology, Delft, the Netherlands

ARTICLE INFO

Keywords:
Toughening strategies
Composite joints
Adhesively bonded joints
And crack deflection

ABSTRACT

Tailoring the stacking sequence of composites bonded joints improves fracture toughness and damage tolerance of the joint by encouraging extrinsic toughening mechanisms, such as crack deflection and crack branching. Previous works show that in composite substrates with tailored laminates, each crack deflection into a new ply can increase the joint's toughness. Still, once a 0° layer is reached, toughness drops abruptly due to sudden delamination. To overcome this limitation, this work explores embedding a co-cured film-adhesive layer to prevent delamination in 0° plies. It examines how the substrate's bending stiffness influences the effectiveness of this toughening strategy. Quasi-static double cantilever beam tests on four different carbon fibre reinforced laminates, with and without the co-cured layer, revealed two regimes: (i) compliant substrates lead to high peel stresses, triggered crack deflection into ±45° plies, enabling bridging and rising R-curves—up to 200% toughness increase; (ii) stiffer substrates suppressed near-tip rotation, and promoted cleavage-like crack growth with minimal toughening.

1. Introduction

The use of adhesively bonded composite joints in safety-critical structures presents challenges, despite their clear benefits, such as uniform load transfer, preservation of fibre continuity, and greater design flexibility [1–3]. Certification of secondary bonding in primary load paths remains limited because adhesively bonded joints can show low tolerance to interfacial defects, sensitivity to crack growth, and potential risk of sudden failure—issues that can be intensified in harsh environments [2–6]. At the same time, reliably detecting “kissing bonds” and weak interfaces remains a challenge for state-of-the-art Non-Destructive Testing (NDT) and Structural Health Monitoring (SHM) methods [3,4,7–11]. For these reasons, backup fasteners are still required in safety-critical areas, despite the weight penalty, which reduces the benefits of composites [2,6].

To facilitate the broader certification and use of adhesively bonded joints, research has focused on toughening strategies that enhance resistance to crack initiation and propagation and delay catastrophic failure during service [12–14].

The adhesive bonding scientific community has been focusing on the development of different toughening strategies: (i) interface and adhesion engineering – techniques such as laser texturing, grit blasting, plasma treatments, or U.V./ozone exposure are being employed to tailor local adhesion by inducing bridging or controlled’ release” features to guide dissipation pathways, thereby enhancing bonded composite joints [15–17]; (ii) intrinsic adhesive toughening – approaches such as curing control or the addition of nano- or micro-reinforcements (e.g., carbon nano tubes and graphene), with graded bondlines, aim to strengthen the adhesive micromechanics, redistribute stresses, increase plastic dissipation and increase fracture toughness [18–25]; (iii) crack-stopping architectures – utilising *Z*-pins, fibre exposure, 3D printed bio-inspired structures (such as overlapping curls), or stop-holes to interrupt, branch, or deflect cracks, providing extrinsic shielding and delaying failure in composite joints [13,26–32].

Besides adhesive-focused strategies, modifying the composite substrates – such as adjusting ply angles, ply thickness, and local lay-up near the bondline – has proven effective [1,33–39]. These modifications help guide the crack path, promote multi-front propagation, and enhance effective toughness in lap and double cantilever beam (DCB) configurations [1,33–36].

* Corresponding author at: IDMEC, Instituto Superior Técnico, Lisbon, Portugal.
E-mail address: rosemere.lima@tecnico.ulisboa.pt (R. A.A. Lima).

https://doi.org/10.1016/j.tafmec.2026.105473
Received 26 November 2025; Received in revised form 11 January 2026; Accepted 19 January 2026
Available online 20 January 2026

Within this substrate-focused approach, the authors' earlier study [1] investigated how tailoring the stacking sequence of Carbon Fibre Reinforced Polymer (CFRP) influences the effective fracture toughness of adhesively bonded DCB specimens under quasi-static mode I loading. Five laminate architectures and two adhesives spanning different toughness levels were examined. That work showed that the ply orientation adjacent to the bondline and the adhesive's fracture toughness jointly govern crack competition and the co-occurrence of multiple damage mechanisms (delamination, cohesive failure, and transverse matrix cracking). Notably, laminates with multi-directional fibre orientations – e.g., $[90/45/-45/0]_s$ and $[90/60/90/-60/0]_s$ – exhibited stepwise increases in effective toughness whenever the crack deflected into a new ply, progressing through the substrate thickness.

However, a common limitation was identified: once the crack reached a 0° ply, delamination occurred, and the R-curve decreased abruptly, reducing the benefits of lay-up tailoring at later propagation stages.

Building on that finding, this work aims to investigate how embedding a co-cured toughening layer just before the final 0° ply can potentially be used as a toughening strategy to prevent delamination of the last 0° ply and preserve toughening during late-stage growth. In addition, this work seeks to experimentally explore how substrate bending stiffness, through its control of near-tip constraint and rotational compliance, governs crack-path selection and the effective activation or suppression of extrinsic toughening mechanisms. By controlling laminate architecture in an experimental setting, this work isolates the role of bending-related constraints and translates these insights into practical guidance for designing toughened adhesively bonded joints.

2. Materials and methods

2.1. Specimens manufacturing

The DCB composite substrates were manufactured using Hexply 8552-AS4, a unidirectional carbon fibre prepreg embedded in a toughened epoxy resin, from Hexcel Composites in Cambridge, UK. The main mechanical properties of the Hexply 8552-AS4 can be found in [1] and are summarised in Table 1.

The bi-component epoxy Araldite 2015/1 (G_{IC} = 640 J/m^2) [30] – supplied by 3 M Scotch-Weld™ – was used as an adhesive for the secondary bond of the DCB specimens. The epoxy film adhesive AF163-2 k (G_{IC} = 2416 J/m^2) [40], with an embedded knit carrier provided by Huntsman International LLC, was used as a co-cured toughening layer in the new, toughened tailored substrate layups. This film adhesive was selected because it offers high toughness, and since it is a film adhesive, it can be easily embedded in the lamination and curing of the composite laminate.

Based on the results of the authors previous article [1], the stacking sequence here studied was $[90/45/-45/0]_S$ and further tailored to include the toughening layer before the last 0-degree ply, i.e. $[90/45/-45/AF/0]_S$, $[90/45/-45/AF/0_3]_S$, and $[90/45/-45/AF/0_5]_S$. The influence of bending stiffness on toughening activation was investigated by adding 0° layers at the midplane of the laminates.

Table 1
Hexply 8552-AS4 materials properties [1,33].

Longitudinal tensile strength (MPa)	2207
Transverse tensile strength (MPa)	81
Longitudinal tensile modulus (GPa)	141
Transverse tensile modulus (GPa)	10
In-plane shear strength (GPa)	114
In-plane shear modulus (GPa)	5.2
Transverse shear modulus (GPa)	3.33
In-plane Poisson's ratio	0.27
Transverse Poisson's ratio	0.5

The CFRP prepreg plies were cut at specific ply angles (90°, 45°, −45°, and 0°) and then stacked together using a hand layup manufacturing method, with intermediate debulking steps between added layers. These debulking intervals were performed in a sealed table under 100 mbar for 20 min each.

After that, the CFRP laminates were placed on a flat aluminium plate covered with an A4000 high-performance fluoropolymer release film (Airtech International Inc., USA) and sealed inside a vacuum bag. The laminates were cured using an autoclave under 5 bars of pressure and a double dwell step: (a) at 110 °C for 60 min and (b) at 180 °C for 120 min. A ramp of 2 °C/min was used between the holding intervals.

Once cured, the CFRP laminates were precisely cut to the DCB specimen's final dimensions (see Fig. 1) by using an automatic COMPCUT ACS machining tool. The smooth side of the laminates was then manually sanded with 400-grit sandpaper in a criss-cross pattern until an even surface was achieved. Finally, the sanded specimen's surface was degreased with an acetone-soaked cloth and exposed to UV light at 40 mm for 7 min to undergo UV/Ozone physical surface treatment. It is worth noting that the UV/Ozone surface treatment is ideal for removing potential organic contaminants and modifying the laminate's surface at a molecular level to improve adhesion [1,30,40].

The specimens were secondary bonded with Araldite 2015/1 and cured in an oven at 80 °C for 60 min. A thermocouple was used to ensure that the adhesive reached the curing temperature, thereby initiating the curing process. An initial crack length (a_0) of 30 mm was maintained by placing a Teflon tape (thickness 0.11 mm) on the bonded side of the substrate's edge. A bond line thickness of 0.3 mm was achieved using thin metallic spacers.

Finally, metallic loading blocks were bonded to the top and bottom surfaces of the specimens using the bi-component epoxy adhesive Araldite 2012, with a curing time of 12 h at room temperature.

In order to analyse the effect of the AF layer on the bending stiffness of the composite laminates, the composite laminates with [90/45/−45/0]S, [90/45/−45/AF/0]S, [90/45/−45/AF/03]S, and [90/45/−45/AF/05]S layups were also cut to produce small samples for 3-point bending tests, measuring 50 ± 0.1 mm in length and approximately 13 ± 0.15 mm in width.

2.2. Experimental setup

Two main experimental tests were performed: (i) 3-point bending test and (ii) DCB quasi-static test under mode I load. For both, a Zwick electro-mechanical testing machine with a 1 kN loading cell was used, and the test specifics are listed below:

(i) 3-point bending test: The specimens were supported by three pins with a 3 mm radius, spanning a total of 30 mm. A testing speed of 1 mm/min was applied, as recommended by ASTM D7264 [41].
(ii) DCB quasi-static test: a testing speed of 4 mm/min was applied in all tests, as recommended by the standard ISO 25217 [42].

At least three specimens of each stacking sequence type were used for each testing series. For the DCB tests, the crack position was monitored through visual inspection of the specimen's lateral surface using a standard digital camera. This inspected surface was painted white to enhance image contrast. Additionally, a millimetre scale was stamped onto the surface to improve crack-tip visualisation and measurement of crack length.

A travelling microscope monitored the remaining lateral free surface of the DCB specimens to capture high-magnification images near the crack propagation paths. Both the regular and travelling microscopes took photographs every 4 s, with recordings synchronised with load and displacement data from the electro-mechanical testing machine. The detailed experimental setup is shown in Fig. 2.

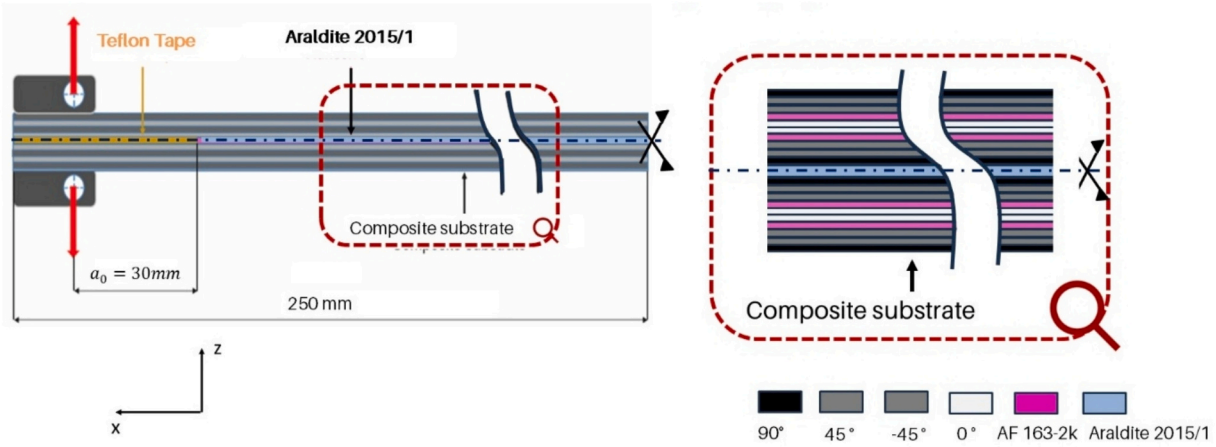

Fig. 1. Specimens' scheme: the dimensions are out of scale.

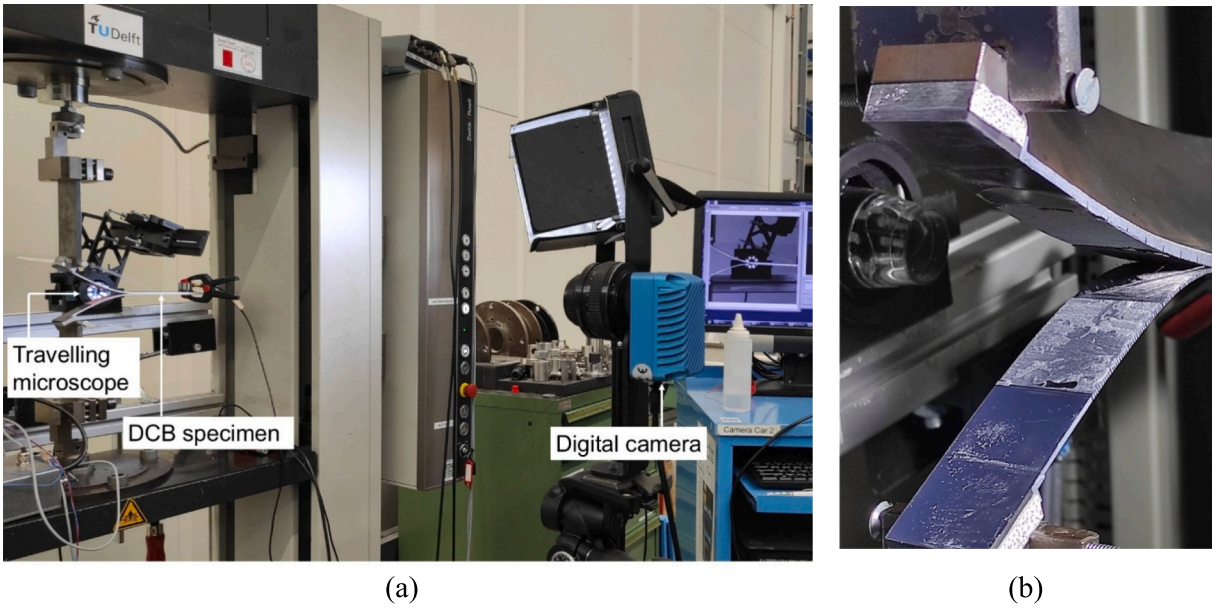

Fig. 2. Experimental quasi-static mode I fracture toughness test and (b) detailed picture of the double cantilever beam specimen during crack propagation.

2.3. Calculation methods: DCB and 3-point bending tests

2.3.1. Modified beam theory

Mode I fracture toughness of each specimen was determined based on the Modified Beam Theory (MBT) as recommended by the standard ISO 25217 [42], following the equation below:

$$G_I = \frac{3P\delta}{2b(a+|\Delta|)} * \frac{F}{N} \tag{1}$$

In which b and a correspond to the specimen's width and crack length measured by visual evaluation, respectively. P and δ are the load (N) and displacement [mm] recorded from the testing machine. This data reduction method uses a calibration parameter (Δ) to account for the specimen's root rotation, experimentally determined by the interception of the least squares fit of the cube root of the specimen's compliance ($C^{1/3}$) as a function of the crack length. Eqs. 2 and 3 were implemented to determine large-displacement (F) and load-block corrections (N).

$$F = 1 - \frac{3}{10}\left(\frac{\delta}{a}\right)^2 - \frac{3}{2}\left(\frac{l_1\delta}{a^2}\right) \tag{2}$$

$$N = 1 - \left(\frac{l_2}{a}\right)^3 - \frac{9}{8}\left[1 - \left(\frac{l_2}{a}\right)^2\right]\frac{l_1\delta}{a^2} - \frac{9}{35}\left(\frac{\delta}{a}\right)^2 \tag{3}$$

Two new variables related to the presence of the loading blocks were introduced in eqs. 2 and 3, which are: l_1 and l_2 which means the distance from the centre of the loading point to the middle plane of the substrate arm to which the block is attached, and the distance between the block edge and the centre of the loading point.

2.3.2. Equivalent bending stiffness

The longitudinal equivalent bending stiffness can be calculated from the 3-point bending tests using Eq. 4, as recommended by ASTM D7264.

$$E_x^f = \frac{\Delta\sigma_f}{\Delta\varepsilon_f} \tag{4}$$

The E_x^f is calculated within a strain range of 0.001 to 0.003. In which $\Delta\varepsilon_f$ represents the difference between the chosen strain values, and the variable $\Delta\sigma_f$ is the difference between the respective stresses in the selected strain points. Stress and strain values were determined taking into account the span length (L), the load versus displacement curve, and

the specimens' dimensions (b – width and h - thickness), following Eqs. 5 and 6, respectively.

$$\sigma_f = \frac{3PL}{2bh^2} \tag{5}$$

$$\varepsilon_f = \frac{3\delta h}{L^2} \tag{6}$$

The equivalent longitudinal bending stiffness E_1^f was also determined using the Composite Laminated Theory (CLT) to be used as a reference, following Eq. (7). For this calculation, the AF163-2 k layer, with a thickness of 0.29 mm, was considered as two layers of the 90° ply, each approximately 0.148 mm thick. The flexural stiffness D_{11} was also determined using CLT after determining the [ABD] matrix of each laminate.

$$E_1^f = \frac{12}{\left(|D_{11}|^{-1} * h^3\right)} \tag{7}$$

In addition to the equivalent longitudinal bending stiffness, the laminate axial stiffness A_{11} was extracted from the [ABD] matrix using CLT. Reporting both A_{11} and D_{11} allows a clear distinction between axial stiffness (A_{11}), which governs load-bearing performance in structural components, and bending-related stiffness (D_{11}), which controls the near-tip constraint in the present fracture configuration.

3. Experimental results

3.1. 3-point bending tests

Table 2 presents the experimentally determined equivalent longitudinal bending stiffness, E_x^f, for each composite laminate, as determined from 3-point bending tests, along with their respective standard deviations. In addition, the corresponding equivalent longitudinal bending stiffness E_1^f determined using the Composite Laminated Theory (CLT) as well as the flexural stiffness D_{11} and axial stiffness A_{11} are shown.

As shown in Table 2, the CLT-calculated values are slightly higher than the experimental values. It is reasonable, as the composite laminate theory does not account for potential defects and geometric irregularities introduced during manufacturing and preparation.

It is also possible to notice that the addition of 0° plies increases both axial and flexural stiffness. However, the scaling differs markedly: A_{11} rises by approximately a factor of three across the investigated configurations, whereas D_{11} increases by more than one order of magnitude.

Fig. 3 plots the bending stiffness, E_x^f, and the flexural stiffness, D_{11}, for each laminate tested.

As shown by comparing the layups $[90/45/-45/0]_S$ and $[90/45/-45/AF/0]_S$, embedding the AF 163-2 k as a toughening layer did not significantly change the bending stiffness. As expected, the highest value of bending stiffness (26.7 GPa) was observed in the specimen with the largest number of 0° layers $[90/45/-45/AF/0_5]_S$. The addition of four more layers at the neutral axis position of the laminate increases the bending stiffness from 18.8 GPa to 26.7 GPa (42% increase).

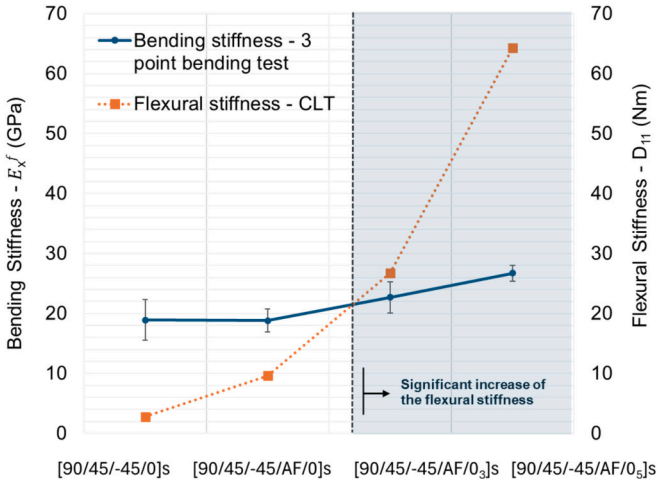

Fig. 3. Experimental results of the 3-point bending test of samples Araldite-90/45 with and without a toughening layer, and analytically obtained flexural stiffness.

A significant increase in flexural stiffness is observed upon adding 0° layers, from 9.6 N/mm to 64.3 N/mm (a 570% increase), as shown in Fig. 3.

There is a significant increase in the specimen's flexural stiffness as a function of the number of 0° plies, reaching a maximum value of 64.3 Nm for the $[90/45/-45/AF/0_5]_S$. These significant differences in flexural stiffness support further analysis of the effect of this parameter on the effectiveness of the toughening mechanism.

3.2. Quasi-static DCB tests

Quasi-static DCB tests were performed for at least four specimens of each stacking sequence configuration. The representative load-displacement curves are shown in Fig. 4. Drawing attention to the presented curves, it is possible to observe that the $[90/45/-45/AF/0_5]_S$ presents the highest maximum load, reaching approximately 190 N compared to the 30 N and 65 N from the specimens without a toughening layer and with only one 0° ply - $[90/45/-45/AF/0]_S$.

It is also worth noting that all curves exhibit different initial stiffnesses, likely due to variations in the flexural stiffness of the substrate arms, as shown in Table 2. Indeed, the least steep curve belongs to the specimen without the AF163-2 k co-cured toughening layer $[90/45/-45/0]_S$, with the lowest $D_{11} = 2.8$ Nm, while the steepest curve corresponds to the $[90/45/-45/AF/0_5]_S$, with the highest $D_{11} = 64.3$ Nm specimen.

The $[90/45/-45/AF/0]_S$ specimen shows a sustained second

Table 2
Layup stacking sequence, equivalent longitudinal bending stiffness, axial and flexural stiffness.

Stacking sequence	Specimen thickness (average ± std) (mm)	Equivalent bending stiffness (E_1^f) – (GPa)		Axial stiffness (A_{11}) – (N/m)	Flexural stiffness (D_{11}) – (Nm)	D_{11}/E_1^f – (m^3)
		3-point bending tests (average ± std)	**CLT theory**			
[90/45/−45/0]s	1.2 ± 0.03	18.9 ± 1.9	22.2	$6.6*10^7$	2.8	0.15
[90/45/−45/AF/0]s	2.09 ± 0.05	18.8 ± 2.6	22.8	$7.3*10^7$	9.6	0.51
[90/45/−45/AF/0_3]s	2.89 ± 0.08	22.7 ± 1.3	28.7	$14.8*10^7$	26.7	1.18
[90/45/−45/AF/0_5]s	3.62 ± 0.09	26.7 ± 3.7	37.2	$22.4*10^7$	64.3	2.41

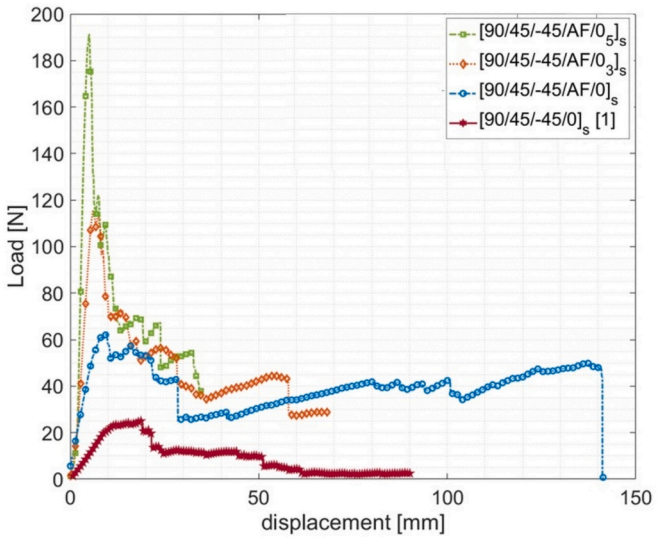

Fig. 4. Representative load versus displacement curve of samples Araldite-90/45 with and without a toughening layer.

increase in the load-displacement curve (after 30 mm of opening displacement), almost reaching the previous maximum load again (50 N) before experiencing an abrupt final failure (see Fig. 4). Specimens $[90/45/-45/AF/0_3]_S$ and $[90/45/-45/AF/0_5]_S$, on the other hand, show a sudden load drop after the peak load, followed by a gradual decrease as a function of the opening displacement. Notably, the specimen without a toughening layer exhibits a very slow reduction in load, followed by multiple plateau regions before ultimately failing.

Fig. 5 shows the typical fracture surfaces for each stacking sequence, accompanied by an illustrative schematic to better understand the crack propagation paths followed. It is worth mentioning that the arrows in Fig. 5 indicate the fibre orientations in each ply. The specimen $[90/45/-45/AF/0]_S$ exhibited a complex fracture surface with multiple crack propagation paths highlighted. Carefully examining Fig. 5 (a), one can observe the onset of cohesive failure marked by the presence of some voids at the beginning of the crack growth direction. This is followed by a crack deflection through the composite substrate mid-plane, with multiple fronts propagating from the 45° to −45° ply, reaching the AF163-2 k co-cured toughening layer, then reversing to the −45° ply and toughening layer until ultimate failure.

A typical fracture surface of the specimens $[90/45/-45/0]_S$ is shown in Fig. 5(b), where a small area of cohesive failure is observed at crack onset, followed by a crack-competition mechanism that leads to the formation of multiple crack fronts, resulting in crack deflection between the 45° and − 45°. as detailed in [1]. The major difference, when compared with the toughened specimen, is the final delamination at the 0° ply observed at the latest stage of its crack propagation. Interesting to note that, in comparison with $[90/45/-45/AF/0]_S$, the final delamination at the 0° ply could definitely be avoided by embedding the co-cured AF163-2 k toughening layer. The $[90/45/-45/AF/0_3]_S$ and $[90/45/-45/AF/0_5]_S$ specimens exhibit 100% cohesive failure behaviour, with the crack propagating within the adhesive layer, as shown in Fig. 5(c).

Fig. 6 (a) shows representative R-curves for the studied layups. Initially, it is possible to observe different values of the effective fracture toughness onset (the point on the R-curve where crack propagation first becomes visible); see the zoom-in in Fig. 6 (b). The specimen without a toughening layer exhibited the smallest onset value, around 650 J/m^2. The specimens with the AF163-2 k co-cured layer showed slightly higher onset values: approximately 770 J/m^2 for specimens $[90/45/-45/AF/0]_S$ and $[90/45/-45/AF/0_3]_S$, and 869 J/m^2 for $[90/45/-45/AF/0_5]_S$,

The specimens that exhibited a cohesive failure, $[90/45/-45/AF/0_3]_S$ and $[90/45/-45/AF/0_5]_S$,display a G effective curve with minor fluctuations (wavy trend) and values ranging from 600 to 800 J/m^2, which are approximately in line with the nominal fracture toughness of the Araldite 2015/1 found in literature (G_{IC} = 600–710 J/m^2 – adhesive thickness in the range from 0.4 to 2.6 mm) [30].

The joints with the $[90/45/-45/0]_S$ layup exhibit a similar behaviour to the specimens $[90/45/-45/AF/0]_S$ with the toughening layer at the very beginning of the crack propagation, from 30 to 35 mm, where both specimens presented a cohesive failure. After that, the behaviour diverges: the specimen with a toughening layer exhibits cohesive failure, whereas the specimen without the toughening layer initiates crack deflection. An accentuated change in crack propagation is observed around 65 mm when the 0° ply was reached, and a full delamination occurred. This led to a significant decrease in the joint's effective fracture toughness for $[90/45/-45/0]_S$ to around 300 J/m^2 at the plateau region of the curve, equivalent to the Hexply 8552-AS4 fracture toughness.

The specimen $[90/45/-45/AF/0]_S$ exhibits an outstanding curve with two increasing stages: (i) from the crack propagation onset until 55 mm of crack propagation, and (ii) from 70 mm until the end of the test. The second stage is very steep, indicating a significant increase in the joint's effective fracture toughness as the crack propagates, with G_{eff} max around 2300 J/m^2, more than double the onset value. This behaviour can be associated with the activation of the toughening layer, as only the specimens with this stacking sequence, the crack reached the AF163-2 k co-cured layer, as observed in Fig. 5.

The parameter Δ reflects deviations from ideal beam-theory compliance arising from near-tip rotations, fracture-process-zone development, and crack-path complexity. In addition, as noted in the author's previous publication [1], the MBT specimen's root rotation calibration parameter (Δ) can also offer valuable insights into the damage evolution phenomena within the specimens and the fracture process zone of the joint, even if a non-pure mode I crack propagation occurs, as in the case of specimens $[90/45/-45/0]_S$ and $[90/45/-45/AF/0]_S$. Despite using the same adhesive across all configurations, significant differences Δ were observed among specimens, reflecting their failure mechanisms and structural configurations (see Table 3).

Specimens exhibiting crack deflection into the composite substrate, such as $[90/45/-45/0]_s$ and $[90/45/-45/AF/0]_s$, showed lower Δ values (1.1 mm and 8.3 mm, respectively), indicating reduced rotational compliance at the crack tip due to energy dissipation within the adherends. In contrast, specimens with fully cohesive failure, such as $[90/45/-45/AF/03]_s$ and $[90/45/-45/AF/05]_s$, exhibited significantly higher Δ values (13.4 mm and 19.4 mm), attributable to larger fracture process zones and increased root deformation caused by higher energy absorption in the adhesive layer. Therefore, a larger Δ indicates larger apparent root rotation and, potentially, larger FPZ under cohesive propagation; meanwhile, a smaller Δ is observed when energy is dissipated in adherends through crack deflection or delamination, reducing the calibration effect of root rotation.

4. Discussion

The discussion is organised into two stages. Sections 4.1 and 4.2 focus on the experimental mechanisms that influence crack-path selection and the activation or suppression of extrinsic toughening in the investigated DCB configurations, with a particular emphasis on the role of the co-cured toughening layer and the effect of substrate stiffness on the effectiveness of the proposed toughening strategy. Building on these mechanistic observations, Sections 4.3 and 4.4 explicitly explore how the identified stiffness effects inform design guidance, clarifying the distinct roles of axial and bending stiffness and formalising the findings into a stiffness–toughness design framework.

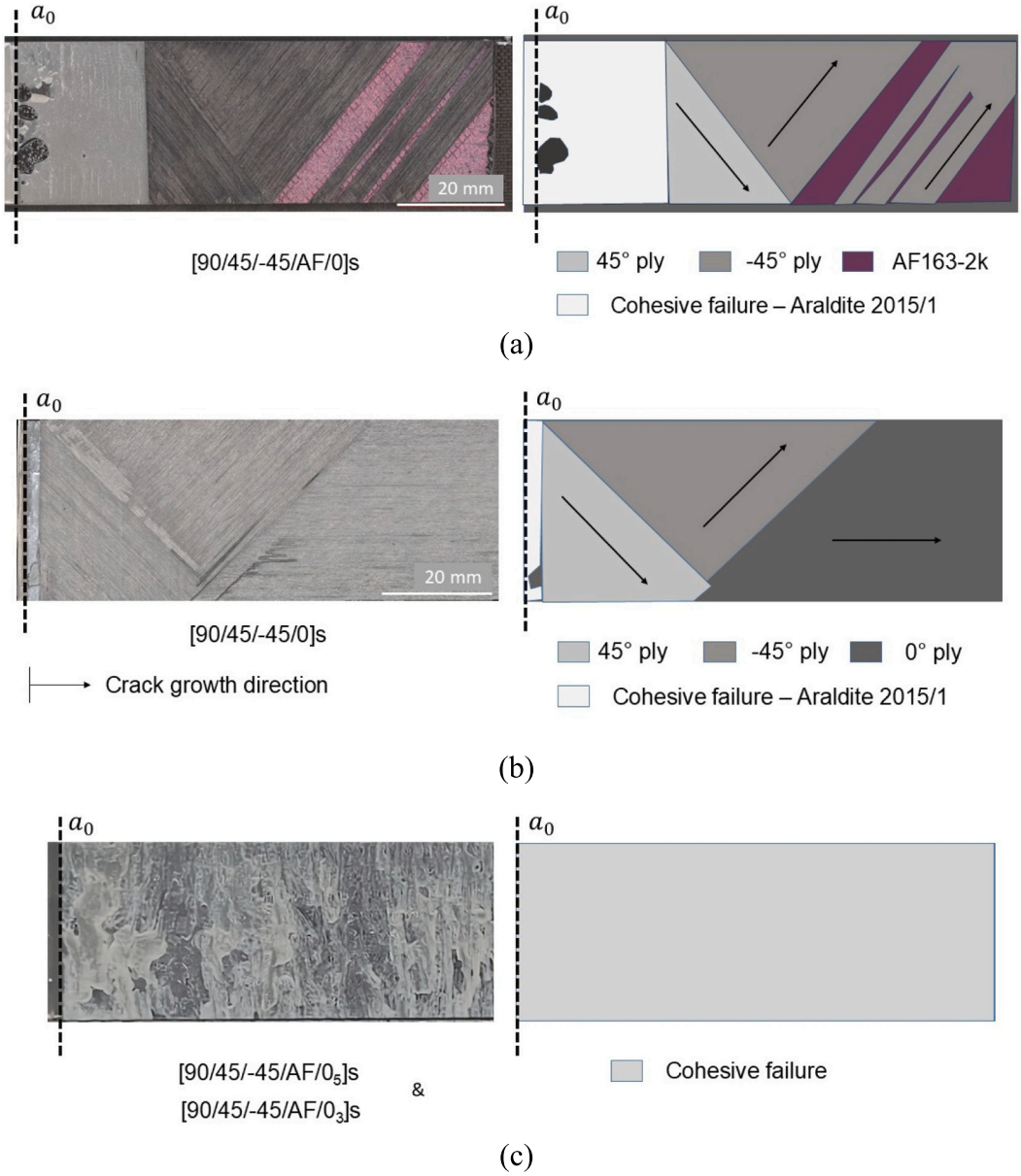

Fig. 5. Fracture surfaces of samples Araldite-90/45 with and without a toughening layer. (Representative photos on the left-hand side and schematics of the fractured paths as a function of the ply directions on the right-hand side).

4.1. Role of the co-cured toughening layer

The AF163-2 k co-cured layer was embedded in the $[90/45/-45/0]_s$ before the last 0° ply to prevent final failure of these composite adhesively bonded joints by sudden delamination and decrease in the joint's fracture toughness in the final phase.

Fig. 7 (a) shows in detail the comparison between the $[90/45/-45/0]_s$ with and without a toughening layer concerning the evolution of effective fracture toughness as a function of the crack propagation. Fig. 7 (b) represents the topography analysis of the fracture surface of the $[90/45/-45/AF/0]_S$, performed with the Keyence VR 5000 wide area profiling system.

As can be seen in Fig. 7 (a), after 60 mm of crack propagation, two different behaviours can be observed:

- Specimen $[90/45/-45/0]_S$ – a plateau around 300 J/m^2 is observed at the G_{eff} curve, consistent with stable crack propagation by delamination at the 0° layer.
- Specimen $[90/45/-45/AF/0]_S$ – a steep rising R-curve is observed, with G_{eff} increasing to >2000 J/m^2. This rise indicates effective activation of extrinsic toughening mechanisms once the crack front reaches the toughening layer (see Fig. 7(b)).

Fig. 7 (b) shows the topography of the $[90/45/-45/AF/0]_S$ specimen with a colour scale varying from 0 to 4 mm. In which the lower limit was defined based on the free surface of the specimen (without any adhesive), and it is the baseline for the specimen's height measurements. As can be seen, the image is divided into three main regions with the transitions indicated by points 1 and 2:

1. Cohesive failure – a slight increase in the R-curve.
2. Crack deflection into the composite substrate – the R-curve shows a drop followed by a recovery, consistent with temporary energy redistribution at ply interfaces [1,37].
3. Crack reaches the toughening layer – huge increase in the R-curve. The crack alternates between the AF163-2 k toughening layer and

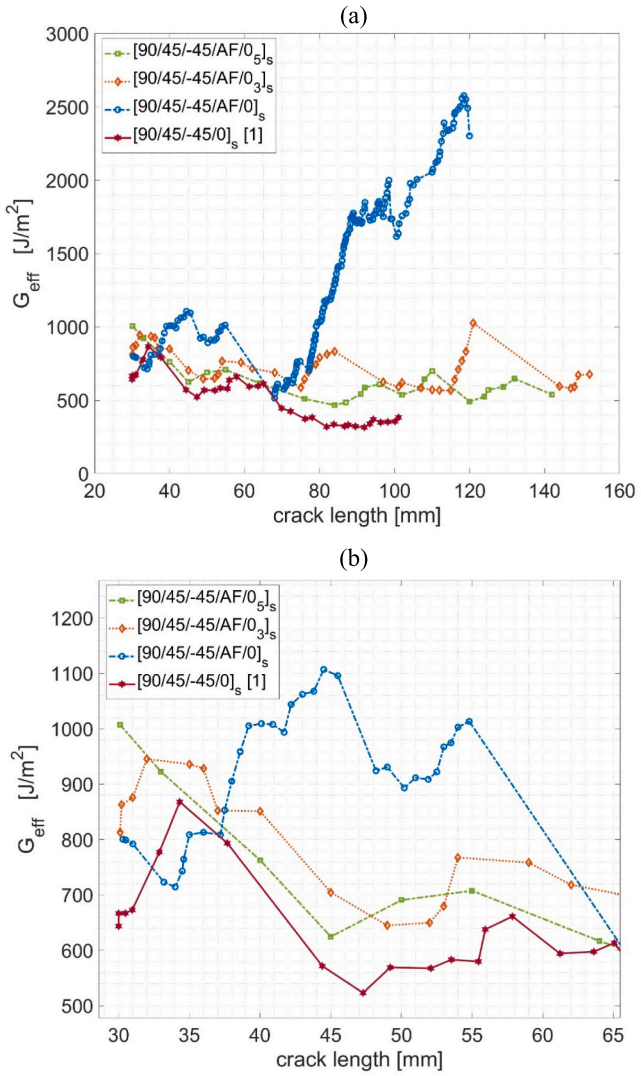

Fig. 6. (a) Representative effective fracture toughness of samples Araldite-90/45 with and without a toughening layer, and (b) zoom in on the onset fracture toughness.

Table 3
Summary of G_{eff} and Δ values for the specimens with and without a co-cured toughening layer.

Specimen type	G_{eff} onset (J/m^2) – average ± standard deviation	G_{eff} max (J/m^2) - average ± standard deviation	Δ(mm)
[90/45/−45/0]$_S$	649 ± 18	771 ± 57	1.1 ± 0.4
[90/45/−45/AF/0]$_S$	769 ± 93	2330 ± 208	8.3 ± 3.9
[90/45/−45/AF/0$_3$]$_S$	763 ± 39	954 ± 79	13.4 ± 2.8
[90/45/−45/AF/0$_5$]$_S$	869 ± 105	937 ± 50	19.4 ± 4.8

the 45° ply, creating multiple interacting crack fronts and enhanced extrinsic toughening, thereby raising the energy required for further propagation.

Carefully analysing the monitoring images taken by the travelling microscope at the free surface of the [90/45/−45/AF163-2 k/0]$_S$ specimens, further insights related to their damage evolution behaviour can be gained, as illustrated in Fig. 8.

As can be seen in Fig. 8, the crack propagation within the composite substrate can be divided into: (i) First stage (from point 1 to point 2 in Fig. 7 (b)) – where the crack propagates in multiple fronts within the substrate, presenting what here is called "step" behaviour. The step behaviour means that the front does not progress monotonically toward the mid-plane but intermittently jumps across adjacent plies and then re-enters previous layers. This tortuous path is potentially promoted by the elastic (stiffness) mismatch between neighbouring layers (e.g., toughening layer and ±45° plies), which redistributes the local stress field at interfaces, increases mode mixity, and favours crack deflection and temporary arrests [37,38].

In the (ii) Second stage – the crack propagation path reaches the toughening layer, with a high toughness and activates another extrinsic toughening mechanism: the AF163-2 k carrier bridging. This extrinsic toughening mechanism constrains the crack faces, retards propagation, and promotes the formation of additional crack fronts and local delamination, as evidenced by the features highlighted in Fig. 8.

Thus, the embedding of a toughening layer and its complete activation created an enhanced crack competition effect, amplified by the elastic (stiffness) mismatch between the substrate layers, which promoted multiple crack propagation fronts and a step-like behaviour. Finally, when the crack reaches the co-cured AF163-2 k layer, beyond its intrinsic higher toughness when compared to delamination, further extrinsic toughening mechanisms are activated, such as the carrier bridging of the adhesive film, which holds the crack propagation longer and consequently increases the energy required for its further development.

4.2. Influence of the substrate's stiffness on the effective activation of the toughening strategy

It was observed that increasing the number of 0° plies in the laminates with the toughening layer entirely altered the damage evolution within the joints, shifting from a complex crack propagation path on specimens [90/45/−45/AF/0]$_S$ to a complete cohesive failure on specimens [90/45/−45/AF/0$_3$]$_s$ and [90/45/−45/AF/0$_5$]$_s$ without engaging extrinsic toughening mechanisms promoted by crack deflection within the composite layer and carrier bridging encouraged by the presence of the co-cured AF163-2 k layer.

The major differences between these layups lie in their flexural stiffness (9.6 Nm of 90/45/−45/AF/0]$_s$ against 26.7 and 64.3 Nm for [90/45/−45/AF/0$_3$]$_s$ and [90/45/−45/AF/0$_5$]$_s$, respectively). From the results, it appears that flexural stiffness plays a major role in triggering crack deflection and, consequently, the toughening effect. To better understand the influence of flexural stiffness on toughening effectiveness, the stresses at the adherent near the crack tip were determined.

Stresses were evaluated using the Winkler elastic foundation method [30,43], in which each adherend is modelled as an Euler-Bernoulli beam supported by a linear elastic foundation representing the adhesive, as represented in Fig. 9. This approach is intended to provide qualitative and comparative insight into how substrate stiffness influences near-tip stress evolution, rather than to predict absolute adhesive stresses.

For the purpose of evaluating near-tip normal stress trends, one adherend is modelled as an Euler–Bernoulli beam supported by a Winkler elastic foundation. This idealisation captures the influence of flexural stiffness on peel-stress evolution in a comparative sense, and hence, only half of the specimen is represented in Fig. 9. In the Winkler-foundation model, each infinitesimal segment of the adhesive layer functions as a linear normal spring, with its reaction proportional to the local separation between the adherend and the rigid substrate (or, in a symmetric DCB, the mid-plane of the joint).

From this, the deflection and rotation along the interface are derived from the equations below, and the adhesive peel stresses are subsequently computed.

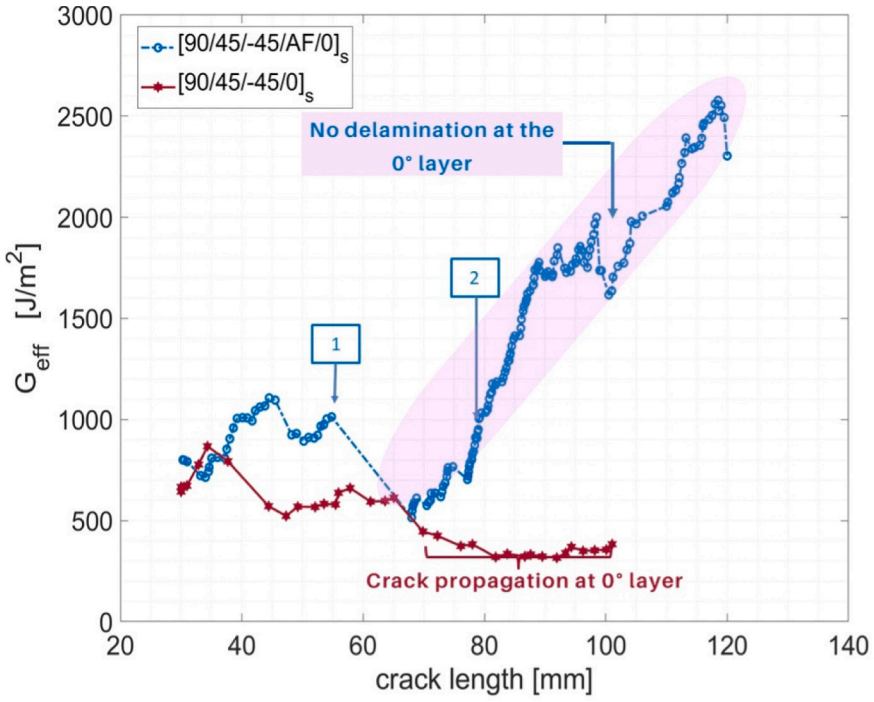

(a)

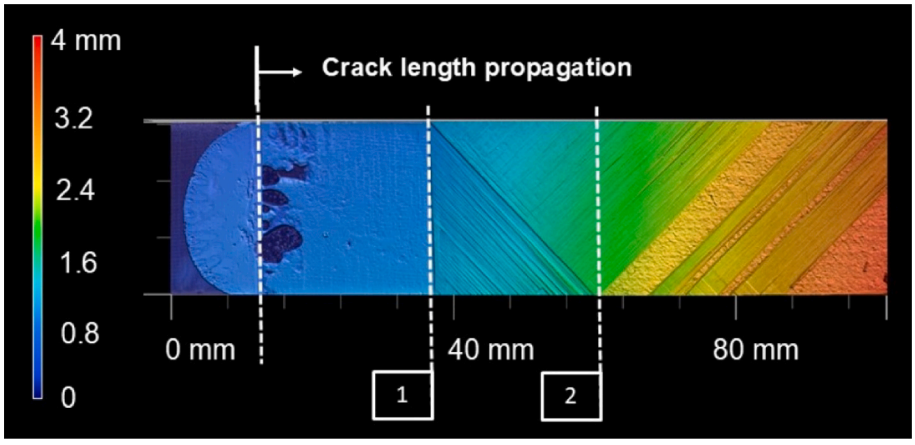

(b)

Fig. 7. (a) Effective fracture toughness of representative specimens with and without toughening layer, and (b) topography of specimen Araldite [90/45/−45/AF/0]s.

The differential equation for the beam in a Winkler foundation is given by,

$$EI\frac{d^4w(x)}{dx^4} = kw(x) \tag{8}$$

where E is the adherend Young's modulus, I *is* the second moment of area, and k is the foundation stiffness per unit of length.

Eq. (9) is derived under the assumptions of linear elasticity, small deflections, uniform adhesive thickness, and perfect bonding between adherends and adhesive. The adhesive stiffness k represents the normal stiffness per unit length of the adhesive layer within the Winkler foundation idealisation.

$$k = \frac{E_a b}{t_a} \tag{9}$$

Where E_a is the adhesive Young's modulus, b the joint width and t_a the adhesive thickness. Given the applied load (P) and a certain crack length (a), the bending moment (M_0) and shear at the crack mouth can be determined, which, in turn, determines the beam solution. The general solution for the deflection w(x) in the bonded region (measured

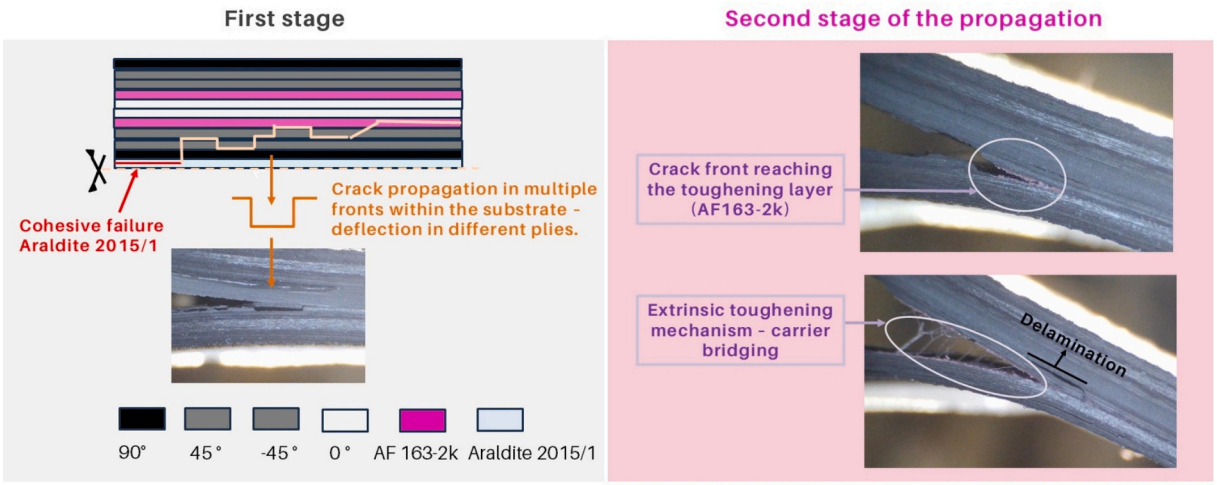

Fig. 8. Schematic of the damage evolution within the specimen Araldite [90/45/−45/AF163-2 k/0]s, including the crack deflections throughout the composite plies and the crack propagation within the toughening layer and final carrier bridging.

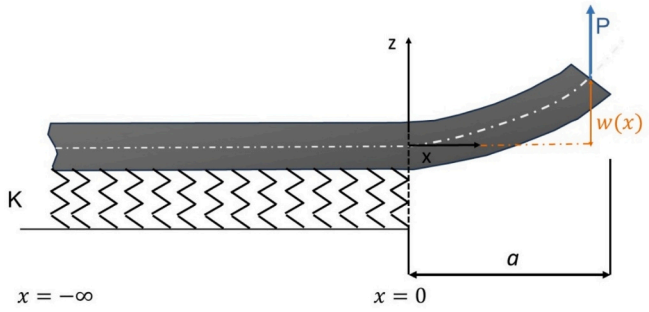

Fig. 9. Scheme Winkler elastic foundation.

from the crack tip, $x = 0$) is the well-known exponentially decaying–oscillatory form [30,43,44]:

$$w(x) = B_1\, e^{\lambda x}\cos(\lambda x) + B_2\, e^{\lambda x}\sin(\lambda x) \tag{10}$$

Where

$$\lambda = \sqrt[4]{\frac{k}{4EI}} \tag{11}$$

This describes the gradual decay of adherend deflection into the bonded zone as the adhesive constrains the beam motion. In addition, B_1 captures how vertical force (shear opening) contributes to the beam deflection field, and B_2 captures the additional rotation or bending caused by the moment at the crack tip, determined by Eqs. 12 and 13.

$$B_1 = \frac{2\lambda}{k}P + \frac{2\lambda^2}{k}M_0 \tag{12}$$

$$B_2 = -\frac{2\lambda^2}{k}M_0 \tag{13}$$

The peel stress in the adhesive is derived by:

$$\sigma_{zz}(x) = \frac{E_a}{t_a}w(x) \tag{14}$$

Physically, E_a/t_arepresents the stiffness of the adhesive layer per unit strain, while $w(x)$ is the relative displacement causing the normal stress. Under the assumption of perfect bonding and small adhesive thickness, $\sigma_{zz}(x)$ corresponds to the normal stress acting on the substrate surface in contact with the adhesive. Therefore, in the following discussion, $\sigma_{zz}(x)$ is interpreted as the interfacial normal stress between adhesive and adherend.

Finally, the normal stresses were normalised following Eq. 15.

$$\widetilde{\sigma_{zz}}(a) = \frac{\sigma_{zz,\mathrm{peak}}(a)}{\sigma_{zz,\mathrm{ref}}} \tag{15}$$

where $\sigma_{zz,\mathrm{peak}}(a)$ is the maximum σ_{zz} evaluated along the surface of the substrate in contact with the adhesive ahead of the crack tip (within a small window of ~1–2 mm) for a given crack length a. The reference value $\sigma_{zz,\mathrm{ref}}$ is the mean peak σ_{zz} measured at the onset.

Fig. 10 compares the normalised peak normal stresses of [90/45/−45/AF/0]s and [90/45/−45/AF/0_5]s, which exhibit complex fracture behaviour with full activation of the toughening strategy and cohesive failure, respectively.

As shown in Fig. 10, the specimen [90/45/−45/AF/0_5]s exhibited an almost flat curve of the normalised peak as a function of crack length. This behaviour is typical in a complete cleavage regime, where a quasi-constant peak peel stress characteristic of self-similar crack growth in a cleavage-dominated regime is observed, characterised here by stable crack propagation and full cohesive failure of the joint [1,45].

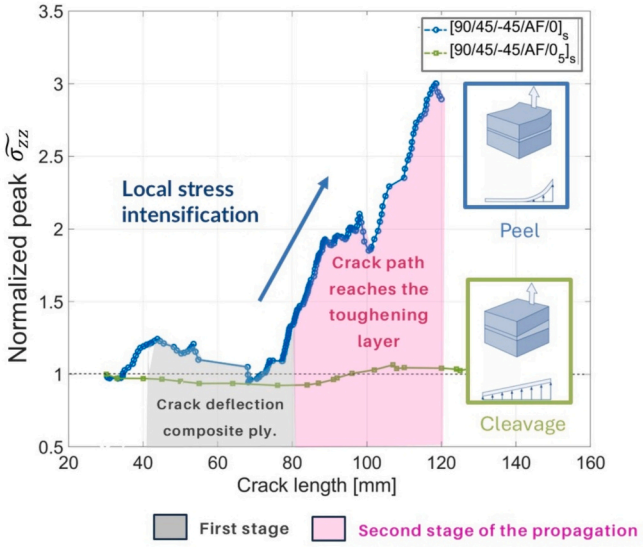

Fig. 10. Normalised values of the substrate's normal stress peaks as a function of the crack length - representative specimens with toughening layer, and different amounts of 0° plies.

In contrast, the curve of the [90/45/−45/AF/0]$_s$ showed an increasing trend from its onset, with waviness in the normalised peak normal stresses during crack deflection within the composite plies (grey region of the graph), followed by a significant increase once the crack reaches the toughening layer (pink area of the graph). This behaviour indicates a shift in the loading regime from cleavage to peel stress, driven by high opening displacement and bending of the arms.

Referring to the 3-point bending results of the laminates, it is clear that an increasing number of 0° plies results in a notable increase in the laminates' flexural stiffness D_{11}. Consequently, a higher D_{11} reduces near-tip rotations and limits mode I peel stresses at the specimen's free surface, thereby confining the crack path and suppressing the stress amplification required to activate the designed toughening strategies.

Therefore, substrate stiffness plays a crucial role in determining whether the crack deflects toward the composite plies and fully activates the intended toughening mechanism by engaging the extrinsic mechanisms (i.e., carrier bridging).

Table 4 summarises the main insights into the effectiveness of the proposed toughening strategy for preventing final delamination at the 0° layer in the [90/45/−45/0]$_s$ laminate, along with its limitations due to elastic mismatch and substrate flexural stiffness.

Finally, it was possible to conclude that the following considerations should be taken into account when designing toughening strategies for composite adhesively bonded joints, with a focus on tailoring the substrates' stacking sequence: (i) influence of ply angles – high ply angles near the bond line increase anisotropy, fostering multi-front propagation [29,37–39]; (ii) elastic mismatches to promote crack-deflection and migration; (iii) flexural stiffness of the substrates.

4.2.1. Assumptions and limitations of the peel-stresses calculation

The Euler-Bernoulli-Winkler model assumes linear elastic behaviour of the adherends, neglects shear deformation and geometric non-linearities, and represents the adhesive as a continuous distribution of linear normal springs. Axial stretching of the adherends and adhesive plasticity are not included.

It is worth noting that the applied Euler-Bernoulli-Winkler model accurately captures the qualitative evolution of stresses and the relative influence of flexural stiffness on the activation of the toughening layer. However, it neglects the stretching effect that occurs when rotations become finite; this effect introduces an additional axial force that stiffens the beam and slightly reduces the predicted deflections and peel stresses. Consequently, at very large openings, the linear Euler-Bernoulli beam formulation may overestimate the local peel stress amplitude and the joint's compliance. Nonetheless, they are applied consistently across all configurations and are therefore suitable for recognising relative trends and transitions between fracture regimes.

Table 4
Summary of the mechanical insights of the bending stiffness effect in triggering the toughening strategy.

Feature	Low Flexural Stiffness [90/45/−45/AF/0]s		High Flexural Stiffness [90/45/−45/AF/0$_3$]s [90/45/−45/AF/0$_5$]s	
Crack deflection	✓	Present	×	Not observed
Stress buildup	✓	Steep rising due to peel stresses	×	Almost flat curve – cleavage mode was observed
Failure mode		Cohesive failure, followed by crack propagation within the substrate plies until final propagation at the toughening layer		Full cohesive failure
Toughening layer effectiveness	✓	Prevented final delamination at the 0-degree ply, holding the crack propagation due to carrier bridging	×	Not reached due to the higher flexural stiffness of the substrates – the crack propagation path was confined within the adhesive layer.

4.3. From test mechanics to design mechanics: Axial stiffness, bending stiffness, and near-tip constraint

Building on the mechanistic observations discussed in Sections 4.1 and 4.2, it is crucial to clarify how the stiffness effects in the DCB configuration should inform design. Previous sections show that substrate flexural stiffness influences crack paths, near-tip rotations, and extrinsic toughening. Still, since these are from bending-dominated tests, their relevance to real structural components, where axial or membrane stiffness is key, must be addressed to avoid test-specific interpretations.

DCB specimens are, by design, bending-driven fracture configurations, in which the elastic energy available for crack growth is supplied primarily through bending and rotation of the substrate arms. Consequently, the specimen compliance, crack-opening displacement, and near-tip stresses are strongly influenced by the laminate flexural stiffness. D_{11}. This characteristic is intrinsic to the test method and does not imply that bending stiffness is, by itself, the dominant design variable in practical bonded structures.

In real composite components, axial (membrane) stiffness governs load-bearing capacity and global deformation, whereas bending stiffness is typically adjusted locally through geometric features such as thickness variation, tapers, or curvature. In this context, bending-related stiffness should be understood not as a global design target, but as a surrogate for the local constraint and rotational compliance at the crack tip, which governs crack-path stability and stress amplification.

In the present study, substrate stiffness is varied through laminate architecture to isolate the role of near-tip constraint within a controlled experimental framework. As shown in Table 2, the addition of 0° plies increases both the axial stiffness $A_{11}$and the flexural stiffness D_{11}. However, their scaling differs significantly. Across the investigated configurations, A_{11}increases by approximately a factor of three (from 6.6 to 22.4 * 10^7 N/m), whereas D_{11}increases by more than one order of magnitude (from 2.8 to 64.3 Nm), reflecting the fundamentally different dependence of axial and bending stiffness on laminate thickness and ply placement.

This difference in scaling is central to the observed fracture behaviour. The transition from crack deflection with carrier bridging in the toughening layer to cleavage-like cohesive propagation does not correlate directly with axial stiffness alone, but instead with the suppression of near-tip rotations and peel-stress amplification caused by large increases in D_{11}.

To synthesise these observations and link test mechanics to design interpretation, the results are summarised in an Ashby-type stiffness–toughness design map, shown in Fig. 11. The map plots axial stiffness A_{11}against the maximum effective fracture toughness $G_{\text{eff,max}}$ in a logarithmic scale, with laminate flexural stiffness D_{11}represented by the colour scale. Marker shape distinguishes the dominant fracture regime, separating crack deflection with carrier bridging within the toughening layer from cohesive propagation.

As shown in Fig. 11, the fracture toughness does not increase monotonically with axial stiffness. Instead, the highest toughness is achieved at intermediate axial stiffness levels (7.3*10^7 N/m), where D_{11}remains sufficiently low (9.6 Nm) to permit near-tip rotations and peel-stress amplification, enabling crack deflection and effective engagement of the co-cured toughening layer.

As axial and flexural stiffness increase further through the addition of 0° plies, near-tip rotations are suppressed, the local loading state becomes cleavage-dominated, and crack propagation remains confined to the adhesive layer. The achievable fracture toughness, therefore, decreases despite higher global stiffness. This representation highlights a constraint-controlled transition between fracture regimes, governed

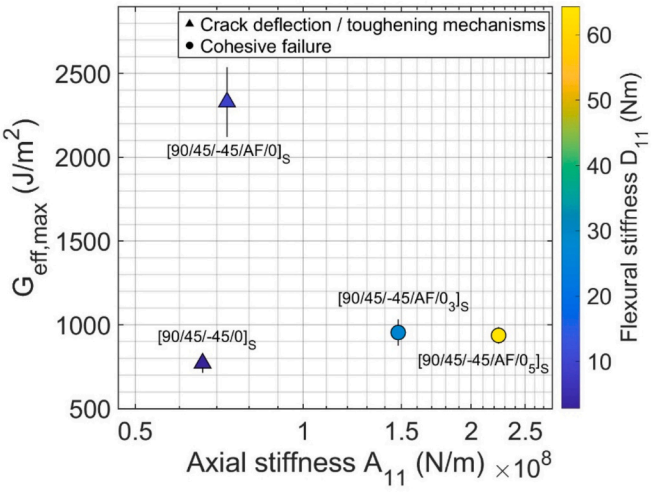

Fig. 11. Ashby-type stiffness–toughness design map.

primarily by flexural stiffness rather than axial stiffness alone.

Overall, the Ashby-type map demonstrates that optimal toughening strategic designs are achieved by preserving axial stiffness while tuning flexural stiffness, and thus near-tip constraint, within a finite window that enables extrinsic toughening mechanisms to operate. Finally, the present Ashby map is populated with laminate-driven stiffness variations; future work may extend it to geometry-driven stiffness variations.

5. Conclusions

This study examines the use of the AF163-2 k co-cured adhesive film as a toughening layer in adhesively bonded composite joints with a $[90/45/-45/0]_s$ laminate stacking sequence to prevent final delamination at the 0° ply and the subsequent reduction in joint fracture toughness. The influence of the substrate's stiffness in effectively triggering the toughening mechanisms was also investigated, and the main conclusions are:

- Role of the AF163-2 k co-cured layer: Embedding AF163-2 k immediately before the 0° ply prevented final 0° ply delamination and produced a steep, rising R-curve once the crack reached the toughening layer, with alternating paths between the co-cured layer and adjacent plies and carrier bridging that delayed growth and increased energy dissipation.
- Elastic mismatch and ply-angle architecture: Elastic mismatch between plies and between laminate and co-cured toughening layer promoted tortuous, multi-front ("step-like") propagation and temporary arrests in $[90/45/-45/AF/0]_s$ specimens.
- Effect of 0° ply content (flexural stiffness increase): Increasing the number of 0° plies substantially raised flexural stiffness (from $D_{11} = 9.6$ Nm for $[90/45/-45/0]_s$ up to $D_{11} \approx 64.3$ Nm for $[90/45/-45/AF/0_5]_s$), which suppressed near-tip rotation and peel stresses and prevented effective triggering of the toughening strategy, resulting in full cohesive failure within the bond line.
- Bending stiffness as a trigger (or suppressor) of toughening: Substrate flexural stiffness governed whether the toughening strategy is activated. Compliant arms enabled crack deflection, triggered toughening-layer interaction, and rising R-curves; stiffer arms confined cracks to the adhesive, resulting in cleavage-like cohesive failure and limited toughness gains.

Lastly, effective toughening requires co-design of (i) substrate stiffness (global and local), (ii) ply-angle placement near the bondline (high angles potentially induce deflection), and (iii) positioning of the toughening layer to avoid undesired sudden delamination and strategically to be reached under loading.

CRediT authorship contribution statement

R.A.A. Lima: Writing – original draft, Visualization, Validation, Methodology, Investigation, Formal analysis, Data curation, Conceptualization. **S. Teixeira de Freitas:** Writing – review & editing, Supervision, Project administration, Methodology, Investigation, Conceptualization.

Declaration of competing interest

The authors declare that they have no known competing financial interests or personal relationships that could have appeared to influence the work reported in this paper.

Acknowledgements

The authors would like to acknowledge Dr. Michele Gulino for supporting the manufacturing of the specimens.

The authors acknowledge Fundação para a Ciência e a Tecnologia (FCT) for its financial support through LAETA (project UID/50022/2025).

Data availability

Data will be made available on request.

References

[1] R.A.A. Lima, R. Tao, A. Bernasconi, M. Carboni, N. Carrere, S. Teixeira de Freitas, Uncovering the toughening mechanisms of bonded joints through tailored CFRP layup, Compos. Part B Eng. 263 (2023), https://doi.org/10.1016/j.compositesb.2023.110853.

[2] A.C. Marques, A. Mocanu, N.Z. Tomi'c, S. Balos, E. Stammen, A. Lundevall, S. T. Abrahami, R. Günther, De Kok JMM, S.T. De Freitas, Review on adhesives and surface treatments for structural applications: recent developments on sustainability and implementation for metal and composite substrates, Materials 13 (24) (2020) 1–43, https://doi.org/10.3390/ma13245590.

[3] M.D. Banea, L.F.M. da Silva, Adhesively bonded joints in composite materials: an overview, Proc Inst Mech Eng Part L 223 (1) (2009) 1–18, https://doi.org/10.1243/14644207JMDA219.

[4] G. Jeevi, S. Kumar Nayak, Kader M. Abdul, Review on adhesive joints and their application in hybrid composite structures, J. Adhes. Sci. Technol. 33 (2019) 1497–1520, https://doi.org/10.1080/01694243.2018.1543528.

[5] K. Tserpes, A. Barroso-Caro, P.A. Carraro, V.C. Beber, I. Floros, W. Gamon, M. Kozłowski, F. Santandrea, M. Shahverdi, Skeji'c D, Bedon C, Rajči'c V., A review on failure theories and simulation models for adhesive joints, J. Adhes. 00 (00) (2021) 1–61, https://doi.org/10.1080/00218464.2021.1941903.

[6] G. Viana, M. Costa, M.D. Banea, L.F.M. da Silva, A review on the temperature and moisture degradation of adhesive joints, Proc Inst Mech Eng Part L 231 (5) (2017) 488–501, https://doi.org/10.1177/1464420716671503.

[7] C. Jeenjitkaew, F.J. Guild, The analysis of kissing bonds in adhesive joints, Int. J. Adhes. Adhes. 75 (2017) 101–107, https://doi.org/10.1016/jijadhadh.2017.02.019.

[8] R.D. Adams, P. Cawley, A review of defect types and nondestructive testing techniques for composites and bonded joints, NDT Int. 21 (4) (1988) 208–222, https://doi.org/10.1016/0308-9126(88)90333-1.

[9] M.G.R. Sause, In situ monitoring of Fiber-reinforced composites, Ssmaterials 242 (2016) 633, https://doi.org/10.1007/978-3-319-30954-5.

[10] C. Kralovec, M. Schagerl, Review of structural health monitoring methods regarding a multi-sensor approach for damage assessment of metal and composite structures, Sensors (Switzerland) 20 (3) (2020) 1–25, https://doi.org/10.3390/s20030826.

[11] M. Saeedifar, M.N. Saleh, S.T. De Freitas, D. Zarouchas, Damage characterisation of adhesively-bonded bi-material joints using acoustic emission, Compos. Part B Eng. 176 (2019) 107356, https://doi.org/10.1016/j.compositesb.2019.107356.

[12] R.A.A. Lima, M. Drobiazko, A. Bernasconi, M. Carboni, On crack tip localisation in quasi-statically loaded, adhesively bonded double cantilever beam specimens by acoustic emission, Theor Appl Fract Mec 118 (2022) 103286, https://doi.org/10.1016/j.tafmec.2022.103286.

[13] C. van Innis, M.K. Budzik, T. Pardoen, Ultra-tough architected adhesive joints for integrated composite processing and bonding, Compos. A: Appl. Sci. Manuf. 177 (2024) 107949. ISSN 1359-835X, https://doi.org/10.1016/j.compositesa.2023.107949.

[14] G. Lubineau, M. Alfano, R. Tao, A. Wagih, A. Yudhanto, X. Li, K. Almuhammadi, M. Hashem, P. Hu, H.A. Mahmoud, F. Oz, Harnessing extrinsic dissipation to enhance the toughness of composites and composite joints: A state-of-the-art

review of recent advances, Adv. Mater. (2024), https://doi.org/10.1002/adma.202407132.
[15] K. Maloney, N. Fleck, Damage tolerance of an architected adhesive joint, Int. J. Solids Struct. 132–133 (2018) 9–19, https://doi.org/10.1016/j.ijsolstr.2017.06.010.
[16] M. Budzik, J. Jumel, Imielinska´K, Shanahan MER., Fracture in composite/aluminium joints of variable adhesive properties, J Adhes 85 (10) (2009) 736–754, https://doi.org/10.1080/00218460902997232.
[17] R. Tao, X. Li, A. Yudhanto, M. Alfano, G. Lubineau, On controlling interfacial heterogeneity to trigger bridging in secondary bonded composite joints: an efficient strategy to introduce crack-arrest features, Compos. Sci. Technol. 2020 (188) (2019) 107964, https://doi.org/10.1016/j.compscitech.2019.107964.
[18] A. Wagih, R. Tao, A. Yudhanto, G. Lubineau, Improving mode II fracture toughness of secondary bonded joints using laser patterning of adherends, Composer Part A Appl Sci Manuf 134 (April) (2020) 105892, https://doi.org/10.1016/j.compositesa.2020.105892.
[19] P. Hu, D. Pulungan, R. Tao, G. Lubineau, Influence of curing processes on the development of fiber bridging during delamination in composite laminates, Compos Appl Sci Manuf 149 (2021), https://doi.org/10.1016/j.compositesa.2021.106564.
[20] A. Güemes, A. Renato Pozo-Morales, A. Fernandez-Lopez, X.F. Sanchéz-Romate, M. Sanchez, Urena ˜A. Strain and damage sensing by CNT modified adhesive films and fibre optic distributed sensing. Comparison of performances in a double lap bonded joint, 2019, pp. 1–6. Available: http://www.ndt.net/?id=25035.
[21] S.H. Yoon, D.G. Lee, In situ crack propagation monitoring in tubular adhesive joints containing quartz nanoparticles, J. Adhes. Sci. Technol. 25 (16) (2011) 1973–1985, https://doi.org/10.1163/016942410X544776.
[22] A.J. Kinloch, J.H. Lee, A.C. Taylor, S. Sprenger, C. Eger, D. Egan, The Journal of Adhesion Toughening structural adhesives via nano-and micro-phase inclusions. (2010), https://doi.org/10.1080/00218460309551.
[23] D. Quan, N. Murphy, A. Ivankovic, Fracture behaviour of a rubber nano-modified structural epoxy adhesive: bond gap effects and fracture damage zone, Int J Adhesion Adhes 77 (May) (2017) 138–150, https://doi.org/10.1016/j.ijadhadh.2017.05.001.
[24] Q. Rao, Z. Ouyang, X. Peng, Enhancing mode I fracture toughness of adhesively bonded unidirectional composite joints using surfactant-stabilised multi-walled carbon nanotube and graphene nanoplate, Polym Test Apr. (2021) 96, https://doi.org/10.1016/J.POLYMERTESTING.2021.107110.
[25] A. Buchman, H. Dodiuk-Kenig, A. Dotan, R. Tenne, S. Kenig, Toughening of epoxy adhesives by nanoparticles, J. Adhes. Sci. Technol. 23 (5) (2009) 753–768, https://doi.org/10.1163/156856108X379209.
[26] R.J.C. Carbas, L.F.M. da Silva, Andr'es LFS., Functionally graded adhesive joints by graded mixing of nanoparticles, Int J Adhesion Adhes Jul. 76 (2017) 30–37, https://doi.org/10.1016/J.IJADHADH.2017.02.004.
[27] D. Quan, N. Murphy, S. Flynn, M. Artuso, C. Rouge, A. Ivankovi'c, Interlaminar fracture toughness of CFRPs interleaved with stainless steel fibres Combining deep learning with computational continuum mechanics (SmartSim) View project Surrogate Lung View project Interlaminar fracture toughness of CFRPs interleaved with stainless steel fibres, 2025, https://doi.org/10.1016/j.compstruct.2018.11.016.
[28] M. Frascio, E.A.S. Marques, R.J.C. Carbas, L.F.M. Da Silva, M. Monti, M. Avalle, Review of tailoring methods for joints with additively manufactured adherends and adhesives, 2025, https://doi.org/10.3390/ma13183949.
[29] M.A. Khan, Development of Rules for the Design of Adhesively Bonded Fibre Reinforced Plastic Composite Joints in Aerospace Applications, 2018.
[30] R. Lopes Fernandes, S. Teixeira de Freitas, M.K. Budzik, J.A. Poulis, Benedictus R. From thin to extra-thick adhesive layer thicknesses: fracture of bonded joints under mode I loading conditions, Eng. Fract. Mech. (2019) 218, https://doi.org/10.1016/J.ENGFRACMECH.2019.106607.
[31] Z. Xu, R. Tao, K. Masania, S. Teixeira de Freitas, Biomimetic toughening design of 3D-printed polymeric structures: enhancing toughness through sacrificial bonds and hidden lengths, Mater. Des. 247 (2024) 113361, https://doi.org/10.1016/j.matdes.2024.113361.
[32] Z. Xu, R. Tao, K. Masania, S. Teixeira de Freitas, Bio-inspired overlapping curl structures for toughening bio-based epoxy: A study on the fracture phenomena, Compos. Sci. Technol. 272 (2025), https://doi.org/10.1016/j.compscitech.2025.111374.
[33] J. Kupski, S. Teixeira de Freitas, D. Zarouchas, P.P. Camanho, R. Benedictus, Composite layup effect on the failure mechanism of single lap bonded joints, Compos Struct 217 (Jun. 2019) 14–26, https://doi.org/10.1016/J. COMPSTR.
[34] A. Ozel, B. Yazici, S. Akpinar, M.D. Aydin, S. Temiz, A study on the strength of adhesively bonded joints with different adherends, Compos B Eng Jun. 62 (2014) 167–174, https://doi.org/10.1016/J.COMPOSITESB.2014.03.001.
[35] L.A. Burns, A.P. Mouritz, D. Pook, S. Feih, Strength improvement to composite T-joints under bending through bio-inspired design, Composer Part A Appl Sci Manuf Nov. 43 (11) (2012) 1971–1980, https://doi.org/10.1016/J.COMPOSITESA.2012.06.017.
[36] B.D. Davidson, R. Krüger, Konig¨M., Effect of stacking sequence on energy release rate distributions in multidirectional DCB and ENF specimens, Eng Fract Mech 55 (4) (1996) 557–569, https://doi.org/10.1016/S0013-7944(96)00037-9.
[37] M.F. Abd Rased, S.H. Yoon, Experimental study on effects of asymmetrical stacking sequence on carbon fiber/epoxy filament wound specimens in DCB, ENF, and MMB tests, Compos. Struct. 264 (2021), https://doi.org/10.1016/j.compstruct.2021.113749.
[38] M.D. Aydin, 3-D nonlinear stress analysis on adhesively bonded single lap composite joints with different ply stacking sequences 84 (2008) 15–36, https://doi.org/10.1080/00218460801888359.
[39] S. Purimpat, R. Jerome, A. Shahram, Effect of fiber angle orientation on a laminated composite single-lap adhesive joint 22 (2013) 139–149, https://doi.org/10.1080/09243046.2013.782805.
[40] S. Teixeira de Freitas, D. Zarouchas, J.A. Poulis, The use of acoustic emission and composite peel tests to detect weak adhesion in composite structures, J Adhes 94 (9) (2018) 743–766, https://doi.org/10.1080/00218464.2017.1396975.
[41] ASTM D7264. Standard Test Method for Flexural Properties of Polymer Matrix Composite Materials. 2021. https://store.astm.org/d7264_d7264m-21.html, 2024.
[42] BS ISO 25217. Adhesives — determination of the mode I adhesive fracture energy of structural adhesive joints using double cantilever beam and tapered double cantilever beam specimens, 2009 https://www.iso.org/standard/42797.html. October 2024.
[43] D.A. Dillard, B. Mukherjee, P. Karnal, R.C. Batra, J. Frechette, A review of Winkler's foundation and its profound influence on adhesion and soft matter applications, Soft Matter 14 (19) (2018) 3669–3683, https://doi.org/10.1039/c7sm02062g.
[44] F. Sun, B.R.K. Blackman, Using digital image correlation to automate the measurement of crack length and fracture energy in the mode I testing of structural adhesive joints, Eng. Fract. Mech. 255, no. June (2021) 107957, https://doi.org/10.1016/j.engfracmech.2021.107957.
[45] A.S. Kojouri, J. Karami, K. Kalteremidou, J. Fan, A. Sharma, Anastasios P. Vassilopoulos, V. Michaud, W. Van Paepegem, D. Van Hemelrijck, An experimental and analytical study of mode I fracture and crack kinking in thick adhesive joints, Compos. Part B Eng. 284 (2024), https://doi.org/10.1016/j.compositesb.2024.111695.